Superalloys 2012: 12th International Symposium on Superalloys
Edited by: Eric S. Huron, Roger C. Reed, Mark C. Hardy, Michael J. Mills, Rick E. Montero, Pedro D. Portella, Jack Telesman
TMS (The Minerals, Metals & Materials Society), 2012

Modeling of the Influence of Oxidation on Thin-Walled Specimens of Single Crystal Superalloys

Matthias Bensch[1], Atsushi Sato[2], Nils Warnken[2], Ernst Affeldt[3], Roger C. Reed[2] and Uwe Glatzel[1]
[1]Metals and Alloys, University of Bayreuth, Ludwig-Thoma-Str. 36b, 95447 Bayreuth, Germany
[2]Department of Metallurgy and Materials, University of Birmingham, Edgbaston, Birmingham, B15 2TT, UK
[3]MTU Aero Engines GmbH, Dachauer Str. 665, 80995 Munich, Germany

Keywords: Oxidation, Modeling, Diffusion, Thin-Walled, Nickel-base Superalloy

Abstract

The microstructural evolution of uncoated single crystal superalloys is modeled taking into account the interplay between oxide growth and substrate response. Experimental investigations demonstrate that γ' fraction of specimens with thicknesses less than 1 mm are strongly affected by oxidation. A model based on thermodynamic and kinetic data only, is presented calculating the growth kinetics of oxide scales and the resulting influence on microstructure evolution of the substrate. The model combines models for oxide growth and substrate response. Currently the main focus is on alumina (Al_2O_3) scale growth as it is the most important oxide for long term behavior. A dynamic growth parameter is used to describe the growth rate of the alumina scale. The model predicts the distribution of the alloying elements as well as the evolution of the generated phases as functions of depth and oxidation time. The model has been applied to three different alloys: the strong alumina forming alloy René N5, the moderate alumina forming alloy M247LC SX and the weak alumina forming alloy SCA425+. Since the γ' fraction is one of the most relevant factors for high temperature creep properties, the present work concentrates on the calculation of the time and space dependent γ' precipitate profile, which is most important for thin wall specimens. The predictions have been verified with very good agreement at an oxidation temperature of 980°C with respect to alumina scale growth and γ' fraction distribution. Predicted and measured alumina scale growth and γ' fraction distribution for oxidation at 980°C are in very good agreement.

Introduction

Single crystal nickel-based superalloys are widely used for most heavily loaded parts in the hottest sections of modern stationary gas turbines and jet engines [1]. Naturally, significant interest exists in weight saving of rotating parts, due to the leverage effect on weight saving of disc, shaft, bearing, casing and thereby overall engine weight. Therefore efforts were made in recent years to reduce turbine blade wall thickness [2-4]. Emphasis on thin-walled parts has to be placed on degradation by oxidation. Many publications [5-8] point out that oxidation plays a major role for the inferior creep performance of thin-walled (< 1 mm) specimens in comparison to regular size specimen (> 5 mm).

Oxidation mechanisms of multi-component single crystal nickel-based superalloys are rather complex. In the case of the superalloy René N5 and at temperatures around 1000°C, a sequence of three different oxide scales forms: a NiO and Co_3O_4 containing outer scale, a multi-phase intermediate layer and next to the substrate a dense and compact alumina (Al_2O_3) layer (see Fig. 1 and 5a). Each of these oxide species influences the overall oxidation kinetics in a subtle and as yet non-quantified way. At the beginning of the oxidation process, oxide growth is observed to be rather rapid, only to slow down later in the process, due to the formation of the continuous Al_2O_3 scale. The extraction of specific alloying elements (especially Al) due to oxide scale formation results in the generation of the γ'-free layer and, further away from the surface, a reduction of γ' fraction [9,10].

The model reported in this paper has been developed with these mechanisms in mind. The rate of alumina formation is of major importance due to its role in changing the oxidation rate and oxidation resistance. The proposed model has to reflect the underlying force-flux equations which drive the diffusion (especially of Al) necessary for oxidation (especially of Al_2O_3) to occur. Of course, the rate of scale formation and depletion of alloying elements underneath the oxide scales are coupled [11-13]. The goal is to predict the dependence of the overall oxidation rate, the extent of the γ'-free layer and the distribution of γ' reduced fraction on alloy composition.

Theory

The microstructure evolution of single crystal nickel-based superalloys in the vicinity of the oxide layer is determined by the interplay between oxide growth and substrate response. The system after oxidation consists of the oxide layer, a specific oxidation affected substrate thickness and the non-affected substrate. In case of thin specimen and sufficient long oxidation exposure (thickness of 0.3 mm, temperature of 980°C, after 6 h), the latter can even disappear completely. The described layered structure forms in all cases. It is obvious that the kinetics of this process depends not only on the driving force of oxide formation, but also on the transport properties of the oxide layer and the substrate. The growth rates of different oxides can differ significantly but the fundamental mechanism of interplay with the substrate is the same. The model illustrated in Fig. 1 couples an oxide growth model (upper part) with a substrate response model (lower part). The lower boundary at $d = 0$ µm is the symmetry axis of an infinite extended (in z-direction) thin sheet.

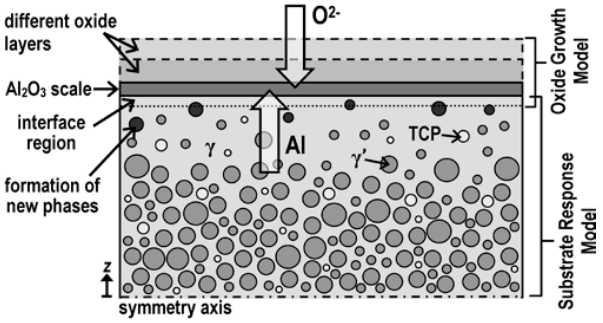

Fig. 1: Diagram of the coupling between oxide growth model with the substrate response model.

Oxide Growth Model

The formation of alumina is the rate-controlling oxidation mechanism. The prediction of the oxidation kinetics is based on two factors: (i) Gibbs free energy ΔG_f (thermodynamic driving force) and (ii) a kinetic factor. Gibbs free energy of alumina

formation is considered as the driving force of oxidation.
(i) In superalloys ΔG_f can be calculated using the natural logarithm of the Al activity, known as Van't Hoff isotherm [14]. The activity of Al is obtained from thermodynamic calculations using ThermoCalc software and TTNi7 thermodynamic database [15-16].
(ii) The transport mechanism in α-Al_2O_3 is known to depend upon the partial pressure of oxygen. For partial pressures < 10^{-5} atm, α-Al_2O_3 becomes an n-type conductor [17] and inward anion transport (O^{2-}) is rate-controlling for alumina growth, while transport of cation (Al^{3+}) can be considered to be negligible. Based on Wagner-Hauffe theory [18] the concentrations of dominant defects are considered to be influenced by impurities [19]. The energy to form α-alumina is estimated to [19]:

$$U = \sum_{i=1}^{n} \left[(z_i - z_{Al}) c_i^{\gamma} \right] \left(\Delta G_f + c_1 \right) \quad (1)$$

where, ΔG_f is the Gibbs free energy of formation of alumina per 1 mol of oxygen, z_i is the valence of element i in the stable i-based oxide (when i = Ni, then z_i = 2 in NiO), and c_i^{γ} is the atomic fraction of element i in the matrix at oxidation temperature. The constant c_1 was determined at 900 and 1000ºC by fitting the chemical compositions which are critical to form a continuous alumina layer by analyzing micro segregation [19]. Using a parabolic growth law for the alumina layer thickness d leads to:

$$d^2 = k_p \cdot t \quad (2)$$

where, t is the exposure time and k_p the parabolic oxidation rate. Fig. 2 summarizes literature data [10,19-23] of the relationship between the energy U to form alumina and the parabolic oxidation rate. Oxidation rates were subdivided into three different groups, corresponding to the representative oxidation rate levels of Al_2O_3, Cr_2O_3 or NiO formation, according to [24]. In case of alumina forming alloys, the mathematical approach to model the parabolic oxidation rate as function of U was chosen as (see Fig. 2a and 2b):

$$k_p = c_2 \cdot e^{(c_3 \cdot U)} \quad (3)$$

where, c_2 and c_3 are temperature dependent constants, which were be obtained by fitting Eq. 3 to data available in literature (CMSX-4 [20], PWA-1484 [20], René N5 (interpolated) and SCA425+0.25Si [19] for 900ºC; CMSX-4 [22], DD32 [23], SCA425+ [19], UCSX-2 [21], René N5 (interpolated for 1000ºC). The parameters are listed in Table 1. Note that two different constants are used.

Table 1: Alloy independent* parameters of equations (1) and (3). (* alumina forming Nickel-Based Superalloy)

	$c_1 \left[\frac{kJ}{mol}\right]$	$c_2 \left[\frac{g}{cm \cdot s}\right]$	$c_3 \left[\frac{mol}{kJ}\right]$	Note
900ºC	551.81	$7.72 \cdot 10^{-5}$	-0.492	-
1000ºC	507.74	$2.45 \cdot 10^{-2}$	-0.566	$U < 50.16$
		$4.86 \cdot 10^{-45}$	1.400	$U > 50.16$

Fig. 3 represents the calculated k_p in comparison to the experimental k_p; indicating the very good agreement of model and experiment. With the described method oxidation rate at two different temperatures can be estimated. The parabolic oxidation rate at other temperatures can be estimated by an Arrhenius type interpolation, marked as triangles in the Fig. 3 for René N5. These values are in good agreement with experimental results. The flux of aluminum J_{Al} into the oxide is given by the oxide growth rate and mass balance. This is the exchange parameter between the oxide growth model and the substrate response model.

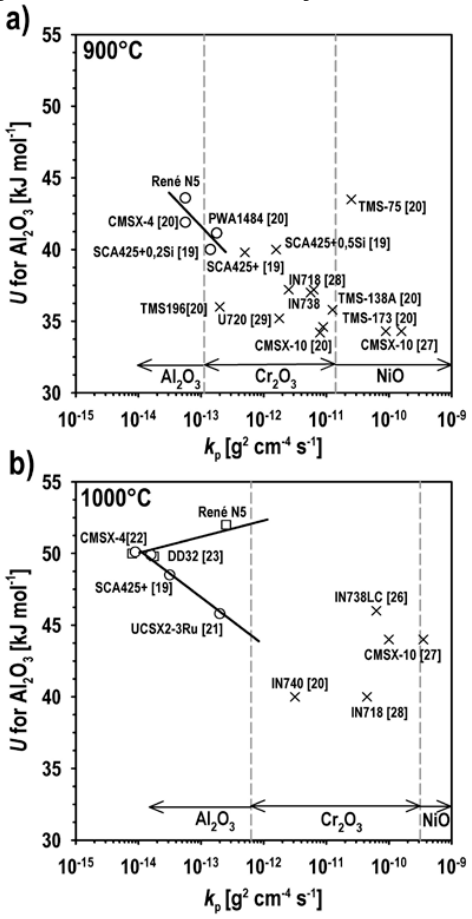

Fig. 2: Parabolic oxidation constant of different nickel-based superalloys taken from literatures[19 - 28] and plotted against the calculated energy U at (a) 900ºC and (b) 1000ºC.

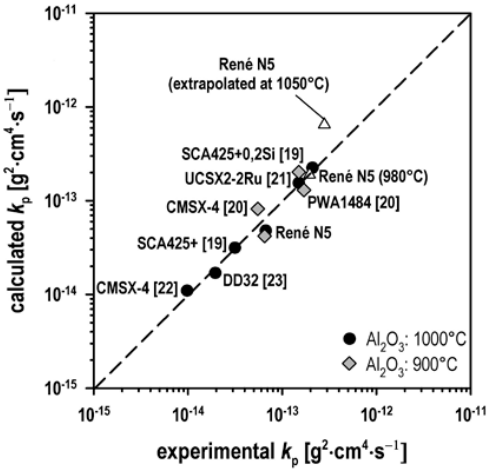

Fig. 3: Calculated parabolic oxidation constant vs. parabolic oxidation constant in literatures. Note that data of selected

alumina forming alloys (CMSX-4 [20,22], PWA1484 [20], SCA425+ [19], UCSX-2 [21], DD32 [23]) are shown.

Substrate Response Model

During the oxidation process the oxide scale formation and growth consumes Al from the substrate. As a consequence, Al has to diffuse from the interior of the substrate towards the oxide/alloy interface (see Fig. 1). The extracted aluminum fraction $x_{matrix,\tau}(Al)$ from the substrate matrix can be calculated for time step τ as:

$$x_{matrix,\tau}(Al) = \frac{M_{\gamma,\tau}}{\rho_{\gamma,\tau}\left(\varepsilon_{\gamma,t_0} - \Delta\varepsilon_{Al_2O_3,\tau}\right)} \cdot \left[x_{matrix,t_0}(Al)\frac{\rho_{\gamma,t_0}\cdot\varepsilon_{\gamma,t_0}}{M_{\gamma,t_0}} - x_{Al_2O_3}(Al)\frac{\rho_{Al_2O_3}\cdot\Delta\varepsilon_{Al_2O_3,\tau}}{M_{Al_2O_3}}\right] \quad (4)$$

where $x_m(Al)$ describes the mole fraction of aluminum in phase m, ρ_m the density, M_m the molar weight and ε_m the expansion. The position of the oxide/alloy boundary moves into the alloy volume. Thereby the distance between the oxide/alloy boundary and the symmetry axis reduces with increasing time t. The thickness reduction $\Delta d(\tau)$ of the specimen is calculated during a time step τ as:

$$\Delta d(\tau) = d_{t-\tau} - \left(\frac{M_{Al_2O_3}}{3M_O\cdot\rho_{Al_2O_3}}\right)\sqrt{k_p\cdot\tau} \quad (5)$$

The diffusion processes in the substrate are simulated by using the DICTRA software and the MobNi1 mobility database [15,29,38]. The activities a_m as well as the concentrations c_i^{γ} of the different alloying elements in the substrate matrix are calculated for the matrix composition of the interface region.

An important factor is the formation of secondary phases. The dispersed phase approach is used [31-32]. This approach is based on the methods of Bongartz et al. [39,40] and Farkas and Ohla [41]. It is assumed that a continuous phase in which one or more dispersed phases exist and only volume diffusion is considered. The calculation is divided into two steps: diffusion process and equilibrium phase formation.

During diffusion, only the composition of the matrix changes. Fraction and composition of the various generated precipitates remain unaffected. Due to the change of matrix composition a change in the overall composition occurs. The mobility N_k of element i can be expressed from the reaction rate by:

$$N_i = \frac{N_i^0}{RT}exp\left(\frac{-Q_i}{RT}\right) \quad (6)$$

where N_i^0 represents the frequency factor and Q_i the activation energy of element i.

The chemical diffusion coefficients $\widetilde{D}_{ij}^{n}$ in a certain phase can be described by equation (7), with the concentration of element n has been chosen as dependent on all other elements [30].

$$\widetilde{D}_{ij}^{n} = \sum_{k=1}^{n-1}(\delta_{ki} - x_i)\,c_k N_k\left(\frac{\partial\mu_k}{\partial x_j} - \frac{\partial\mu_k}{\partial x_n}\right) \quad (7)$$

with δ_{ki} the Kronecker delta function and x_i, x_j and x_k the mole fraction of element i, j and k.

Using the chemical diffusivity the flux J_k of element k can be written as:

$$J_k = -\sum_{j=1}^{n}\widetilde{D}_{kj}^{n}\frac{\partial c_j}{\partial z} \quad (8)$$

The concentration gradient of element j in z-direction is given by $\frac{\partial c_j}{\partial z}$. The dispersed phases act as point sinks or sources of solute atoms in the simulation and their fraction and compositions are calculated from the overall composition [33]. The precipitations also act as obstacles for matrix diffusion, by partly blocking the diffusion path, resulting in a longer diffusion distance. The change of Al concentration varies the chemical potential of all other alloying elements. Therefore, other alloying elements will also start to diffuse due to cross diffusion effects [34].

For diffusion calculations in dispersed systems, Engström [35] recommends the use of bounds proposed by Hashin and Shtrikman [36]. In a two phase system with phase fractions f_1 and f_2, a big difference in diffusivity of an element exists. The upper and lower bounds of the effective diffusivity have been calculated in [36]. If $D_1 \gg D_2$ the upper D_u and lower D_l bounds are given by [37]:

$$D_u = D_1\left(\frac{2f_1}{3-f_1}\right) \quad \text{for} \quad f_1 \geq f_2 \quad (9)$$

$$D_l = D_2\left(1 + 3\frac{f_1}{f_2}\right) \quad \text{for} \quad f_1 < f_2 \quad (10)$$

The term in the brackets is called labyrinth factor. In the substrate response model the labyrinth factor is changed according to the precipitate fractions between eq. 9 and 10. With this approach the composition profiles of all alloy elements as a function of oxidation time can be calculated. The dispersed phase approach is described in Fig. 4.

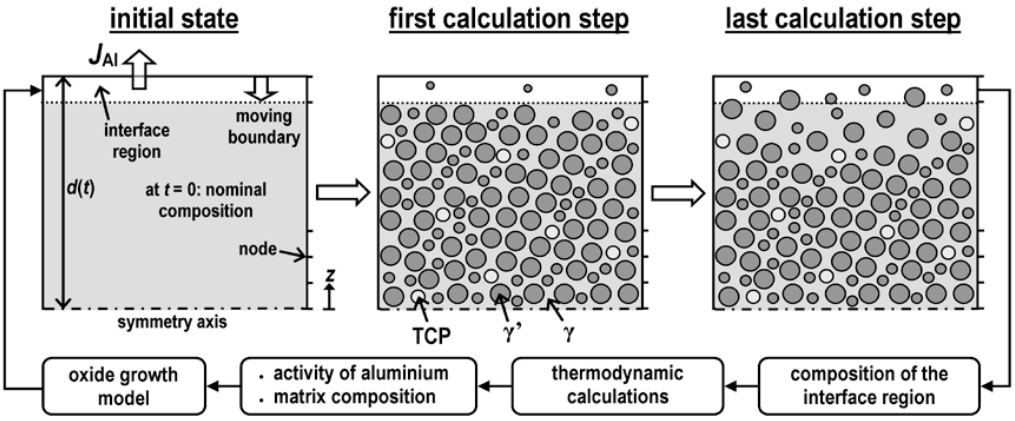

Fig. 4: Schematics description of the modeling concept

Table 2: Measured composition [wt. %] of the investigated single crystal nickel-based superalloys.

Alloy	Al	Cr	Co	Hf	Mo	Ni	Re	Ta	Ti	W
M247LC SX	5.8	8.1	9.3	1.4	0.5	61.5	-	3.3	0.7	9.4
René N5	6.2	7	8	0.2	2	61.1	3	6.5	-	5
SCA425+	4.6	15.5	5	0.1	1	61.8	-	8	-	4

The left image of Fig. 4 shows the initial state of the one dimensional simulation (z-direction). It is defined by a volume with the nominal composition of the alloy at time $t = 0$ h. Due to the symmetric structure only one half of the specimen is considered. The area is divided in a sequence of different parallel layers defined by the distance between two nodes. The upper part of the specimen is bordered by the oxide/alloy boundary. The lower part is bordered by the symmetry axis ($d = 0$ µm) which is the centre of the sheet. Next to the oxide/alloy boundary an interface region is defined. The width of this region is given by the distance of two nodes.

The first step of calculation is shown in the centre of Fig. 4. Based on the databases TTNi7 [16] and MobNi1 [38] the formation of different phases can be calculated. In order to reduce both the computational time and to guarantee the stability of the calculation the number of possible generated phases has been limited to: fcc matrix , γ'-phase and three TCP-phases (P-, R- and µ-phases). Due to similar densities of γ'-phase and matrix, the mole and volume fraction are considered to be identical.

The completed simulation (Fig. 4: right image) shows a new element concentration depth profile. The element concentrations in the interface region is communicated to the oxide growth model.

For the next time step of the substrate response model a new element concentration of the interface region is given by the oxide growth model. The calculation procedure of the substrate response model is repeated for constant increments of time until the desired computed oxidation time t is reached. The time step size is chosen such that no discontinuities from the oxidation growth model are transferred to the substrate response model leading to a stable numerical solution.

Material and Experimental Procedure

Three single-crystal nickel-based superalloys have been chosen: the strong alumina scale forming alloy René N5, the moderate alumina scale forming alloy M247LC SX and the weak alumina scale forming alloy SCA425+. The compositions are given in Table 2. In order to investigate the oxidation performance, specimens ($20 \cdot 15 \cdot 1.1$ mm^3) were prepared from an ingot using an electric wire discharge machine (EDM). The samples are then vibration ground with 1200 abrasive paper (SiC-paper) down to thicknesses of 1.0 mm, 0.3 mm and 0.1 mm and cleaned with acetone. The specimens are placed in an Al_2O_3 crucible and isothermally oxidized in ambient air in a preheated furnace at 980°C. After 100 h the oxidized specimens are removed from the hot furnace and cooled down under ambient conditions. For microstructure analysis the oxidized samples are embedded in resin and polished.

The sample cross sections have not been etched. The area fraction of the γ' phase is determined by the quadrant back scattering detector (QBSD) in a Zeiss 1540EsB scanning electron microscope (SEM) from volumes of equal distance d from the symmetry axis. For each distance the recorded images are binarized manually and the γ' fraction determined. Thickness determination and phase identification have been performed using energy dispersive X-ray spectroscopy (EDX) in the SEM and X-ray diffraction (XRD) technique.

Oxidation Behavior of René N5, M247LC SX and SCA425+

Fig. 5a) shows the oxidized surface of René N5 after 50 h at 980°C. René N5 forms a sequence of three different oxide scales: A top oxide layer consisting of NiO with a small content of Co_3O_4, a multiphase interlayer (α-Al_2O_3, Cr_2O_3, $NiTa_2O_6$, TaO_2, $NiCr_2O_4$, $NiAl_2O_4$, $CoTa_2O_6$) and next to the alloy a dense and compact α-alumina layer denoted as bottom oxide layer. The oxide scale formed on SCA425+ after oxidation for 25 h at 980°C is shown in Fig. 5b). This scale can be separated into four different oxide layers: first a Cr_2O_3 containing top oxide layer, a second oxide layer consisting of Ta_2O_5; a $Ni(Cr,Al)_2O_4$ and Ta_2O_5 containing third oxide layer and finally a bottom oxide layer consisting of pure α-Al_2O_3.

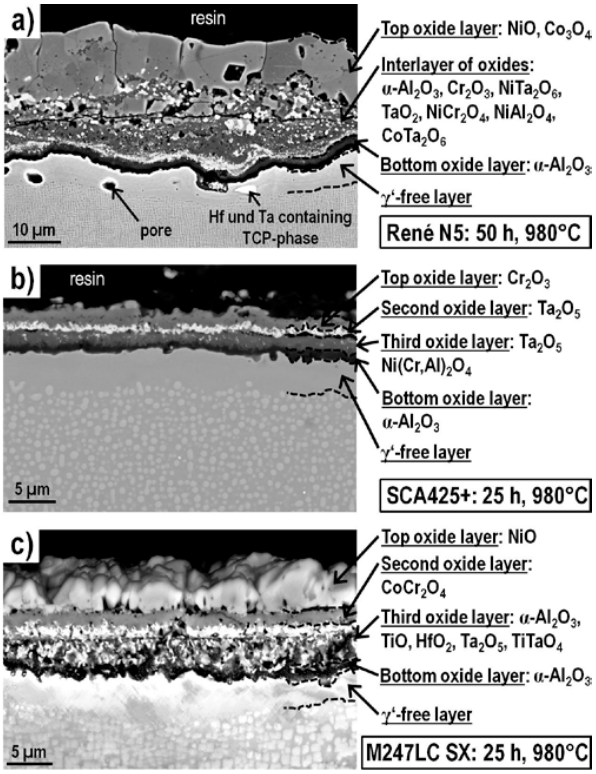

Fig. 5: Oxide scales formed on substrates of René N5 after 50 h (a), SCA425+ after 25 h (b) and M247LC SX after 25 h (c). The alloys have been oxidized at 980°C in ambient air. Note the difference in length scales.

The oxide layer forming on M247LC SX after an oxidation time of 25 h at 980°C can be separated into four different layers (Fig. 5c): A NiO containing top oxide layer, a second oxide layer ($CoCr_2O_4$), a third oxide layer (α-Al_2O_3, TiO, Ta_2O_5, $TiTaO_4$, HfO_2) and close to the substrate a continuous α-Al_2O_3 layer. A

γ'-free layer was observed underneath the bottom oxide layer for all three alloys.

γ' Morphology

The evolution of the γ' morphology of 1.0 mm thick René N5, M247LC SX and SCA425+ specimens oxidized for 100 h at 980°C is shown in Fig. 6 with identical magnification. The images on the left hand side (Fig. 6 a – c) show the γ' morphology evolution of René N5, in the centre of M247LC SX and on the right hand side (Fig. 6 e – h) of SCA425+, for different distances *d* from the symmetry axis. The images Fig. 6 c), f) and i) show the microstructure at the symmetry axis and the images a), d) and g) show the microstructure underneath the γ'-free layer.

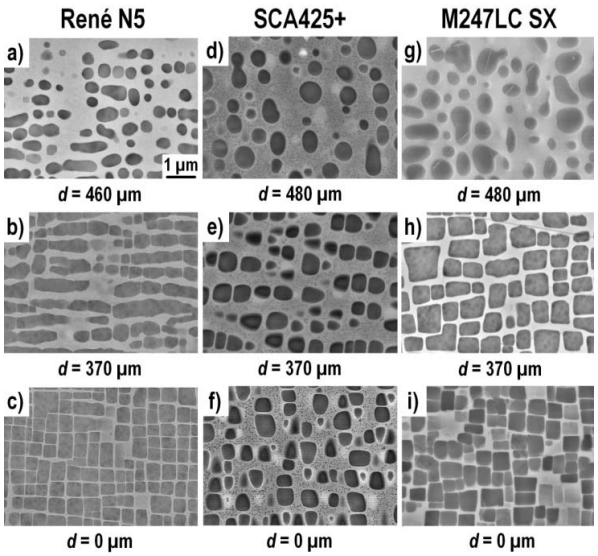

Fig. 6: Evolution of the matrix/γ' microstructure of 1.0 mm thick René N5, SCA425+ and M247LC SX specimens after oxidation at 980°C for 100 h (ambient air) in dependence of the distance *d* to the symmetry axis. The SEM-images show the microstructure in identical magnification.

Fig. 6c) shows the regular cubic γ' structure of René N5. This morphology changes with increasing distance from the symmetry axis in a coarse cubic or rafted structure (d = 370, Fig. 6b). Finally, near the γ'-free layer (d = 460 µm, Fig. 6a), coarse spherical structures are observed. Fig. 6f) shows the initial γ' morphology of SCA425+ with a lower γ' content and less regular morphology than René N5. For d = 370 µm (Fig. 6e) no significant difference can be observed. For distance d = 480 µm (Fig. 6d) the shape of the γ'-phase changes in a spherical structure and a reduced γ' content can be observed. M247LC SX shows a regular cubic γ' morphology (Fig. 6i) with a γ' content in-between René N5 and SCA425+. With increasing distance from the symmetry axis this morphology changes into a regular cubic but coarsed γ' structure (d = 370, Fig. 6h). Near the γ'-free layer (d = 480 µm, Fig. 6g), coarsed and spherical shaped γ' structure are observed.

Measured γ' fraction

Fig. 7 shows the measured γ' fraction as function of distance *d* from the symmetry axis. The measurements are indicated by the different symbols. Fig. 7 shows the measured γ' fraction of René N5 (a), SCA425+ (b) and M247LC SX (c) oxidized for 100 h at 980°C in ambient air. The line thickness correlates with the substrate thickness (1.0 mm: thick line, 0.3 mm: intermediate line thickness, 0.1 mm: hairline).

The experimental data of René N5 1.0 mm specimen (Fig. 7a) reveal a reduction of the γ' fraction of about 250 µm. A reduced γ' fraction for d = 250 - 480 µm underneath a 30 µm thick γ'-free layer for 480 - 500 µm (1.0 mm, 980°C, 100 h). The remaining sample thickness shows no reduction of γ' content.

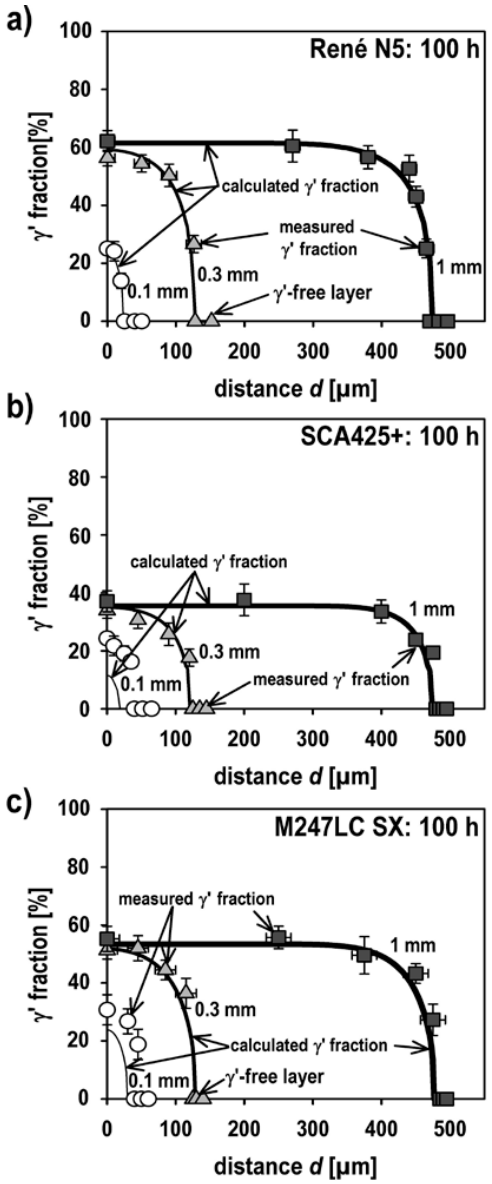

Fig. 7: Measured γ' fraction (symbols with error bars) of Renè N5 (a), SCA425+ (b) and M247LC SX (c) specimens oxidized at 980°C for 100 h in ambient air. The γ' distribution calculated by the proposed model is given by a thick line for 1.0 mm specimens, by a medium line thickness for 0.3 mm specimens and by a hairline for 0.1 mm specimens.

Already for the 0.3 mm specimen the γ' fraction is reduced over the entire specimen, at the symmetry axis down to 57% from 62% of the unoxidized sample in thermodynamic equilibrium. The 0.1 mm specimen shows an even stronger decrease down to 29%. Additionally, the 0.1 mm samples shows an increased thickness of the γ'-free layer (~ 35 µm as compared to ~ 20 µm for thicker samples). SCA425+ (Fig. 7 b) and M247LC SX (Fig. 7c) oxidized at 980°C for 100 h reveal a similar trend, but with lower impact.

The alloy SCA425+ (Fig. 7b) shows for all thicknesses after (Fig. 7c) a small γ'-free layer (< 20µm). Within the scatter no reduction of the initial γ' fraction at the symmetry axis can be observed for 1.0 mm specimen. Only a 80 - 100 µm wide region near the γ'-free layer shows a significant reduction of γ' fraction. Merely for the 0.1 mm specimen the γ' fraction is affected in the entire thickness resulting in a γ' fraction at d = 0 µm of 25% from initially 36% of the unoxidized specimen with the nominal composition in thermodynamic equilibrium.

The measured γ' fractions of 1.0 mm specimens of M247LC SX (Fig. 7c) offer a 200 µm (d = 300 - 480 µm) wide oxidation affected region with reduced γ' fraction underneath a 20 µm thick γ'-free layer. The entire cross section of 0.3 mm M247LC SX specimen shows a reduced γ' fraction. At the symmetry axis a reduction of the γ' fraction from initially 57% down to 54% is observed. The measurements of 0.1 mm specimen offer a reduction of γ' fraction down to 30% at the position of the symmetry axis.

It can be summarized: René N5 exhibits the strongest influence of oxidation on γ' fraction followed by M247LC SX and SCA425+.

Simulation results

In order to calculate the γ' fraction distribution, all alloying elements of Renè N5 M247LC SX and SCA425+, as listed in Table 2, have been considered. An initial node distance of 2 µm has been used as space grid.

Predicted Alumina Scale Growth

The computed alumina scale growth (black dashed lines) on René N5, M247LC SX and SCA425+ for 980°C up to 100 h is shown in Fig. 8. In case of René N5 (Fig. 8a), after a calculated oxidation time of 100 h, an alumina scale thickness of 2.6 µm at 980°C are predicted.

In case of SCA425+ (Fig. 8b), the predicted behavior is quite different. After building up an alumina scale of 0.6 µm (980°C) within a very short time period of time (< 1 h), the alumina thickness stays nearly constant.

The alloy M247LC SX (Fig. 8c) shows a delayed growth of the alumina scale – at 980°C a delay of 5 h is observed. Afterwards a continuous Al_2O_3 layer forms with a thickness of 1.5 mm after 100 h.

The present work uses a dynamic oxide scale growth parameter $k_{Al_2O_3}$, unlike the more traditional approach of assuming a constant. The calculated alumina growth parameters of different alloys (René N5: solid line, M247LC SX dashed line, SCA425+: dotted line) as functions of time are shown for 980°C in Fig. 9.

A decreasing value of $k_{Al_2O_3}$ with increasing time is observed for all alloys. René N5 and M247LC SX show similar behavior - a sharp drop within the first two hours followed by a stationary process. This transition results from the rapid changing composition within the interface region (Fig. 4). For SCA425+ a very steep drop of $k_{Al_2O_3}$ is observed during the first hour of oxidation. After about 30 h oxidation the alumina growth parameter of SCA425+ reaches a nearly constant value of 10^{-8} µm² h^{-1}.

Predicted γ' Fraction Profiles of René N5

The calculated γ' fraction distribution at 980°C is exemplarily plotted for René N5 in Fig. 10. The upper plot shows 1.0 mm substrate thickness, the middle 0.3 mm and the lower 0.1 mm. The array of curves represents different time steps of the simulation process, with t in-between 0 and 100 h.

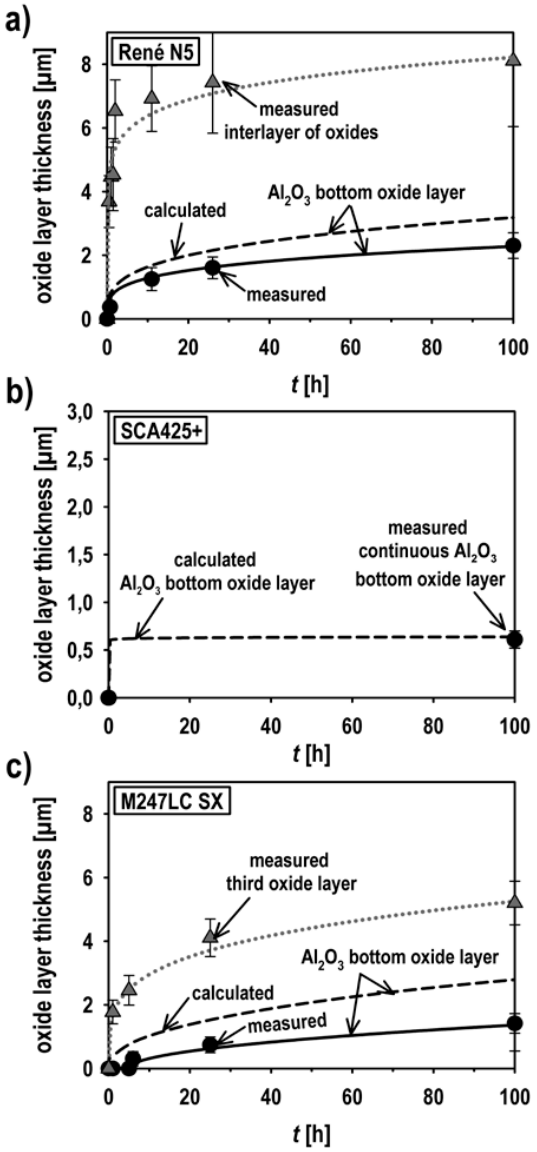

Fig. 8: Comparison of measured (black solid lines) and computed (black dashed lines) alumina layer growth on René N5 (a), SCA 425+ (b) and M247LC SX (c) at 980°C in ambient air. If present, the experimentally determined growth of other aluminum containing oxide layers (Fig. 5) is shown (grey dotted lines), see a) and c).

For a calculated oxidation time t = 0 h at 980°C (Fig. 10) a step function with an equilibrium γ' fraction of 62% is predicted by the ThermoCalc calculations. With increasing time not only a reduction of γ' fraction is observed for all substrate thicknesses, but also the formation of a γ'-free layer.

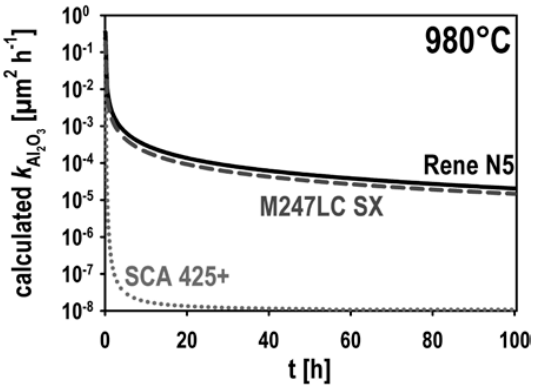

Fig. 9: Calculated alumina growth parameter $k_{Al_2O_3}$ as a function of oxidation time. The growth constant was computed at 980°C for René N5 (solid line), M247LC SX (dashed line) and SCA425+ (dotted line)

The calculations for Renè N5 at 980°C (Fig. 10) show, that at t = 100 h the influenced region expands to more than 200 µm. The calculations for Renè N5 at 980°C (Fig. 10) show, that at t = 100 h the influenced region expands to more than 200 µm. Therefore, the part of the specimen, which has not been affected by oxidation is 0.6 mm or 60% of initial thickness. Already within the first 10 h a 7 µm wide γ'-free layer forms. The calculated results of the 0.3 mm specimen reveal, that the total specimen thickness has been influenced by oxidation after 48 h. Up to 100 h the calculated initial γ' fraction decreases to 58% and a 18 µm wide γ'-free layer is formed. In case of the 0.1 mm already after 5 h the total thickness is influenced by oxidation. The computations reveals a decrease in γ' fraction to 42% after 50 h and to 24% after 100 h.

Discussion

Due to different modeling concepts, parameters and alloys, a comparison of the presented model with published models [42-45] is not straight forward. Suzuki et al. [45] formulated pure empirical equations predicting the initial oxidation behavior of nickel-base superalloys forming different oxide scales based on weight change measurements. The physics based thermodynamic kinetic oxidation models of Nijdam et al. [42,43] take external oxidation of the most alloy constituents in multicomponent (up to five constituents) multiphase alloys and the reaction of the substrate into account. Unlike in the present work, both models use parabolic oxide scale growth kinetics [42] or combined linear and parabolic [43] oxide scale growth constants. In contrast to the use of constants Saltykov et al. [44] model the formation and growth of a sequence of different oxide scales on binary and ternary alloys as a sequence of different local phase equilibria.
Therefore we compare our simulated results with experimental data of: alumina growth and γ' fraction distribution profiles.

Comparison of Model Predictions with Experimental Results of Alumina Scale Growth

Fig. 8 shows the comparison of predicted and experimentally determined growth behavior of the alumina layer forming on René N5 (Fig. 8a), SCA425+ (Fig. 8 b) and M247LC SX (Fig. 8 c) at 980°C. Solid lines with circles represent the experimentally obtained thicknesses, dashed lines the calculated thicknesses. The growth behavior of further alumina containing oxide layers (Rene: Interlayer of oxides, M247LC SX: Third oxide layer) is indicated by grey dotted lines with triangles, see Fig. 5.
In case of the alloy SCA425+, Sato et al. [19] have observed different morphologies of the Al_2O_3 scale in dendritic and interdendritic regions, which is related to variations in local composition. A continuous Al_2O_3 scale is preferentially observed at interdendritic regions, due to higher Al-concentration.

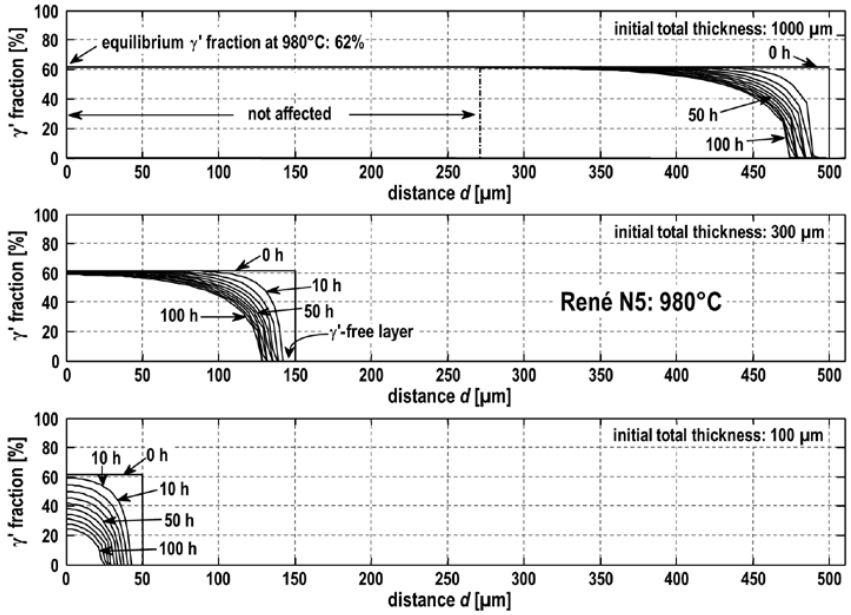

Fig. 10: Calculated evolution of the γ' fraction of Renè N5 at 980°C in dependence of the initial total substrate thickness. Top down, the initial total substrate thickness reduces from 1000 µm to 100 µm. Each graph shows the γ' fraction as a function of the distance d for different time steps.

Very good agreement between the measured continuous alumina scale and the computed alumina thickness on SCA425+ (Fig. 8 b) is observed.
Discrepancies between measured and calculated thicknesses are found for René N5 (Fig. 8 a) and M247LC SX (Fig. 8 c). Experimental observations reveal that not only the continuous alumina layer contains α-Al_2O_3, but also two further oxide layers - the interlayer of oxides (René N5) and the third oxide layer (M247LC SX). In the calculations, the alumina fraction within the interlayer of oxides is considered to be part of the alumina layer, which leads to thicker predicted alumina layers than experimentally observed.
Another reason for this difference can be found in the oxide growth model. The model takes only the conductivity mechanisms of the most stable and simple oxides into account. Complex oxide structures like spinel are neglected. Since the interlayer of oxides includes in addition to α-Al_2O_3 a high number of mixed oxides and spinels, the discrepancy between the measured and calculated values of alumina layer thickness of René N5 at 980°C can be explained.
It can be summarized that the model describes the oxide layer thicknesses for all three alloys (René N5, SCA425+ and M247LC SX) at 980°C with sufficient accuracy.

Comparison of Model Predictions with Experimental Results of γ' Fraction

The calculated γ' fraction (exemplarily plotted for René N5 in Fig. 10) is compared with the measured γ' fraction of all three alloys and thicknesses after 100 h oxidation at 980°C, see Fig. 7. The different symbols show the measured and the solid black lines the calculated γ' fraction.
A very good agreement between experiment and model is observed. A discrepancy is found only for the alloys SCA425+ and M247LC SX at 980°C and 100h for 0.1 mm sample thickness (Fig 7 b and c hairline). A reason for the difference of very thin samples (0.1 mm) is the accuracy of sample preparation which is in the range of 10 µm.
The number of generated phases has been limited in the simulations in order to decrease computation time and increase stability. In order to check the validity of this approximation, calculations have been performed allowing all possible phases to develop. Only in the case of René N5 µ-phases are formed additionally with a very low fraction of < 2.5%. Therefore it can be summarized, that all thermodynamic relevant phases have been considered in the simulation.
The comparison of René N5, M247LC SX and SCA425+ at 980°C up to 100 h is shown in Fig. 11. The curves describe the reduction of the oxidation unaffected specimen thickness in dependence of time.
Despite the lower initial γ' fraction of SCA425+ (36%) and M247LC SX (56%) compared to René N5 (62%) the results show that SCA425+ and M247LC SX are better suited for thin-walled structures than René N5, because these alloys form a thinner continuous alumina scales than René N5. This results in a reduced Al extraction by the oxide layer from the substrate.
Despite the alloy-dependent differences an entirely affected cross section is observed for 0.1 mm initial specimen thickness in 1 - 6 h and for 0.3 mm in 21 - 49 h. The time dependence for the distances from the surface ($d_{initial}$ - $d(f_{\gamma', threshold})$) to reach three different γ' fraction threshold values (57%, 31% and 0%, from initially 62%) is plotted for an 0.1 mm René N5 specimen at 980°C in Fig. 12.

Due to the strong aluminum consumption during oxidation René N5 has been selected for this analysis. After oxidizing for only 5 h (the vertical dotted line) the entire specimen thickness of 0.1 mm is affected by oxidation, resulting in a γ' fraction reduction by 5% and deviation from thin sample behavior from thick (several mm, dashed curve) sample behavior. As soon as the initial γ' fraction at the symmetry axis is influenced by oxidation, a deviation from thick-walled specimen behavior can be observed leading to an accelerated γ' fraction reduction of the thin-walled specimen. The thickness dependence of different γ' fraction threshold values (62%, 57%, 31%) reaching at a specific time a defined distance of 50 µm from specimen surface is shown for 980°C in Tab. 2.

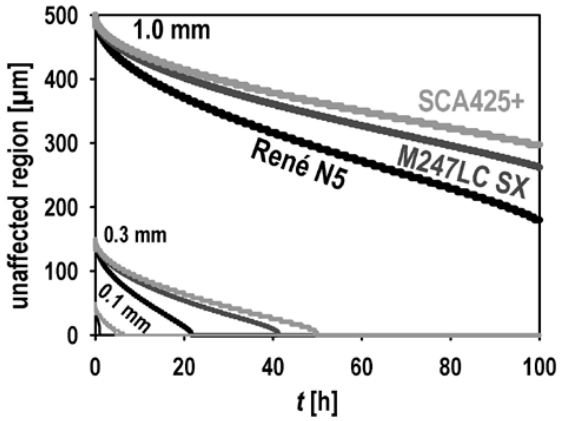

Fig. 11: Calculated oxidation unaffected specimen thickness for different initial specimen thickness in dependence of time at 980°C. The reduction of the unaffected region is described for SCA425+ by the grey lines, for M247LC SX by the dark grey lines and for René N5 by the black lines.

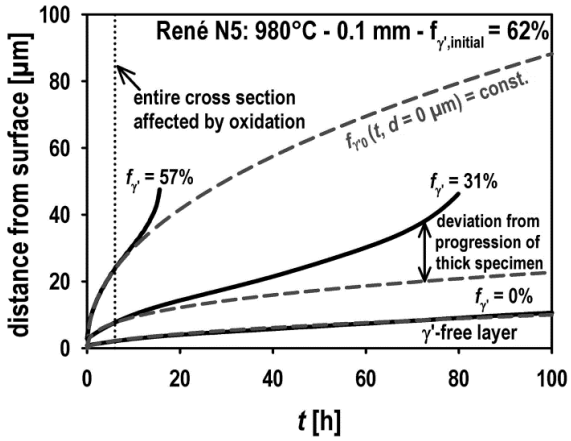

Fig. 12: Calculated progression of different γ' fraction threshold values (57%, 31% and 0%) within an oxidation affected 0.1 mm René N5 specimen at 980°C for times up to 100 h. The initial γ' fraction of the untreated specimen is 62%. The dashed lines indicate the calculated progression of different γ' fractions (57%, 31% and 0%) of an several mm thick specimen.

Up to a period of 5 h oxidation thin- (0.1 mm) and thick-walled (> 1 mm) structures show identical behavior. From this point there is a significant temporal acceleration of the decrease of different γ' fraction threshold values of thin structures (e.g. for 57% γ' fraction 15.5 h in contrast to 27.5 h). This deviation increases with decreasing γ' fraction.
The limited Al reservoir has the strongest influence on different oxidation behavior of thin-walled specimen in comparison to thick specimen. The alloy dependent build up rate of alumina is thereby responsible for a different thin-walled influence.

Conclusion and Outlook

A coupled thermodynamic-kinetic model, based on thermodynamic and kinetic data and on three oxidation parameters c_i only, is presented to calculate the alumina layer growth and the influence of oxide scale formation on γ' morphology of thin-walled specimens (γ'-free and γ'-reduced layer). The predicted behavior is compared to oxidation tests carried out on the alloys René N5, M247LC SX and SCA425+ at 980°C and can be summarized to:

- A model has been developed describing alumina growth and influence of oxidation on γ' fraction as function of oxidation time, temperature and specimen thickness. All relevant thermodynamically stable phases are considered.
- Oxidation has a strong influence on morphology and γ' fraction distribution as function of depth of thin-walled specimens (0.1 - 1.0 mm).
- Measurements and calculations offer that the γ' fraction of René N5 is strongly affected by oxidation. M247LC SX and SCA425+ show similar behavior but with a lower impact.
- The limited aluminum reservoir influences the formation of γ'-free layer and γ'-reduced layer.

The advantage of the combined model is that oxide scale thicknesses, γ'-free layer and γ' fraction as function of distance to the surface can be predicted with high accuracy for alumina forming nickel-based superalloys. Input parameters needed are

- thermodynamic and kinetic databases
- Values c_1, c_2 and c_3 of equation (1) and (3)
- alloy composition
- time and temperature of oxidation exposure.

Thereby it is possible to calculate γ' fraction and elemental distribution of thin-walled specimens as function of time, temperature, location and alloy composition.

Outlook

Based on predictions of the presented model and the knowledge of creep behavior of γ'-reduced layers, the high temperature creep performance of thin-walled turbine blades can be calculated and used as valuable information for turbine blade design with loss of metal cross section accounted for.

References

[1] R.C. Reed, "The superalloys: fundamentals and applications" (Cambridge U.K.: Cambridge University Press, 2006).

[2] Y. Shigemichi, "Thin-walled, lightweight cooled turbine blade" (US Patent 20040091360 A1, 2003).

[3] G. Liang, "Thin turbine rotor blade with sinusoidal flow cooling channels" (US Patent 7753650 B1, 2010).

[4] K.F. O'Connor: "Single-cast, high-temperature thin wall gas turbine component" (US Patent 5545003, 1996).

[5] B. Cassenti and A. Staroselsky, "The effect of thickness on the creep response of thin-wall single crystal components", Mater Sci Eng A, 508 (2009), 183–189.

[6] M. Doner and J.A. Heckler, "Identification of mechanisms responsible degradation in thin-wall stress-rupture properties", Superalloys 1988, ed. S. Reichman, D.N. Duhl, G. Maurer, S. Antolovich, C. Lund (Warrendale, PA: The Metallurgical Society (TMS), 1988), 653-662.

[7] R. Hüttner, J. Gabel, R. Völkl and U. Glatzel, "Creep behavior of thick and thin walled structures of a single crystal nickel-base superalloy at high temperatures – experimental method and results", Superalloys 2008, ed. R.C. Reed, K.A. Kenneth, P. Caron, T.P. Gabb, M.G. Fahrmann, E.S. Huron, S.A. Woodard (Warrendale, PA: The Metallurgical Society (TMS), 2008), 719-726.

[8] R. Hüttner, J. Gabel, U. Glatzel and R. Völkl, "First creep results on thin-walled single-crystal superalloys", Mater Sci Eng, A 510-511 (2009), 307-311.

[9] M. Wenderoth, R. Völkl, S. Vorberg, Y. Yamabe-Mitarai, H. Harada and U. Glatzel, "Microstructure, Oxidation Resistance and High-Temperature Strength of γ' Hardened Pt-Base Alloys", Intermetallics, 15 (2007), 539-549.

[10] M. Bensch, J. Preussner, R. Huttner, G. Obigodi, S. Virtanen, J. Gabel and U. Glatzel, "Modelling and analysis of the oxidation influence on creep behaviour of thin-walled structures of the single-crystal nickel-base superalloy René N5 at 980°C", Acta Mater, 58 (2010), 1607-1617.

[11] D.P. Whittle, D.J. Evans, D.B. Scully and G.C. Wood, "Compositional changes in the underlying alloy during the protective oxidation of alloys", Acta Metall, 15 (1967), 1421-1430.

[12] B.D. Bastow, D.P. Whittle and G.C. Wood, "Alloy Depletion Profiles Resulting from the Preferential Removal of the Less Noble Metal During Alloy Oxidation", Oxid Met, 12 (1978), 413-436.

[13] H.E. Evans, A.T. Donaldson and T.C. Gilmour, "Mechanisms of Breakaway Oxidation and Application to a Chromia-Forming Steel", Oxid Met, 52 (1999), 379-402.

[14] N. Saunders and A. Miodownik, "CALPHAD (Calculation of Phase Diagrams): A Comprehensive Guide", (Kidlington, U.K.: Elsevier Science Ltd, 1998).

[15] J.O. Andersson, T. Helander, L. Höglund, P.F. Shi and B. Sundman, "Thermo-Calc and DICTRA, Computational tools for materials science", Calphad, 26 (2002), 273-312.

[16] Thermotech Ni-based Superalloys Database, TTNI7, Version 7.0, Thermo-Calc Software AB, Stockholm, Sweden, 2006.

[17] P. Kofstad, "Nonstoichiometry, Diffusion and Electrical Conductivity in Binary Metal Oxides", (Malabar, FL: Robert E. Krieger, 1983).

[18] C. Wagner, "The Mechanism of the Decomposition of Nitrous Oxide on Zinc Oxide as Catalyst", J Chem Phys, 18 (1950), 69-71.

[19] A. Sato, Y.L. Chiu and R.C. Reed, "Oxidation of nickel based single-crystal superalloys for industrial gas turbine applications", Acta Mater, 59 (2011), 225-240.

[20] K. Kawagishi, A. Sato and T. Kobayashi, "Oxidation Properties for 2^{nd}-5^{th} Generation Ni base Single-crystal Superalloys at 1023, 1173 and 1373 K", J Japan Inst Metals, 71 (2008), 313-321.

[21] I.M. Edmonds, H.E. Evans and C.N. Jones, "The Role of the γ' Precipitate Dispersion in Forming a Protective Scale on Ni-Based Superalloys at 750°C, Oxid Met, 73 (2010), 193–206.

[22] M. Göbel, A. Rahmel and M. Schütze, "The Isothermal-Oxidation Behavior of Several Nickel-Base Single-Crystal Superalloys with and Without Coatings", Oxid Met, 39 (1993), 231-261.

[23] C.T. Liu, X.F. Sun, H.R. Guan, Z.Q. Hu, "Oxidation of the single-crystal Ni-base superalloy DD32 containing rhenium in air at 900 and 1000°C", Surf Coat Technol, 197 (2005), 39-44.

[24] B. Gleeson, "High Temperature Corrosion of Metallic Alloys and Coatings", Corrosion and Environmental Degradation of Materials, ed. M. Schütze (Weinheim, Germany: Wiley-VCH, 2000).

[25] M.S. Pampana, "Study of Characteristics of Plasma Nitriding and Oxidation of Superalloy IN738LC", (Master Thesis, Louisiana State University, 2004).

[26] S.R. Hegde, "High Temperature Oxidation Behaviour of the Single Crystal Superalloy CMSX-10" (Master Thesis, The University of British Columbia, 2005).

[27] G.A. Greene and C.C. Finfrock, "Oxidation of Inconel 718 in Air at High Temperatures", Oxid Mat, 55 (2001), 505-521.

[28] J.H. Chen, P.M. Rogers and J.A. Little, "Oxidation Behavior of Several Chromia-Forming Commercial Nickel-Base Superalloys", Oxid Met, 47 (1997), 381-410.

[29] DICTRA Version 24, ThermoCalc Software AB, Stockholm, Sweden; 2006.

[30] J.-O. Andersson and J. Ågren, "Models for numerical treatment of multicomponent diffusion in simple phases", Journal of Applied Physics, 72 (1992), 1350-1355.

[31] A. Engström, L. Höglund and J. Ågren, "Computer simulation of diffusion in multiphase systems", Metall Mater Trans A, 25 (1994), 1127-1134.

[32] T. Helander and J. Ågren, "Computer simulation of multicomponent diffusion in joints of dissimilar steels", Metall Mater Trans A, 28 (1997), 303-308.

[33] A. Borgenstam, A. Engström, L. Höglund and J. Ågren, "DICTRA, a Tool for Simulation of Diffusional Trasnformations in Alloys", Journal of Phase Equ, 21 (2000), 269-280.

[34] S. Wöllmer, T. Mack, M. Göken, S. Zaefferer and U. Glatzel, "Characterization of Phases of Aluminized Nickel Base Superalloys", Surf Coat Technol, 167 (2003), 83-96.

[35] A. Engstöm, "Interdiffusion in multiphase, Fe-Cr-Ni diffusion couples", Scandinavian Journal of Metallurgy, 24 (1995), 12-20.

[36] Z. Hashin and S. Shtrikman, "A variational approach to the theory of the effective magnetic permeability of multiphase materials", J Appl Phys, 33 (1962), 3125-3131.

[37] T. Gómez-Acebo, B. Navarcorena and F. Castro, "Interdiffusion in multiphase, Al Co Cr Ni Ti diffusion couples", J of Phase Equil and Dif, 25 (2004), 237-251.

[38] TCS Ni-alloys Mobility Database, MOBNi1, Version 1.0, Thermo-Calc Software AB, Stockholm, Sweden; 2006.

[39] K. Bongartz, D.F. Lupton and H. Schuster, "A model to predict carburization profiles in high temperature alloys", Metall Trans A, 11 (1980), 1883-1893.

[40] K. Bongartz, W.J. Quadakkers, R. Schulten and H. Nickel, "A mathematical model describing carburization in multielement alloy systems", Metall Trans A, 20 (1989), 1021-1028.

[41] D. Farkas and K. Ohla, "Modeling of diffusion processes during carburization of alloys", Oxid Met, 19 (1983), 99-115.

[42] T.J. Nijdam and W.G. Sloof: "Modelling of composition and phase change in multiphase alloys due to growth of an oxide layer", Acta Mater, 56 (2008), 4972-4983.

[43] T.J. Nijdam, L.P.H. Juergens and W.G. Sloof, "Modelling the thermal oxidation of ternary alloy-compositional changes in the alloy and the development of oxide phases", Acta Mater, 51 (2003), 5295-5307.

[44] P. Saltykov, O. Fabrichnaya, J. Golczewski and F. Aldinger, "Thermodynamic modeling of oxidation of Al-Cr-Ni alloys", Journal of Alloys and Compounds, 381 (2004), 99-113

[45] A.S. Suzuki, K. Kawagishi, T. Yokokawa, H. Harada and T. Koboyashi, "Prediction of initial oxidation behavior of Ni base single crystal superalloys by regression analysis", Scripta Mater, 65 (2011), 49-52.